MICROSTRUCTURE IMPACT ON THE MACHINING OF TWO GEAR STEELS. PART 1: DERIVATION OF EFFECTIVE FLOW CURVES

Gottfried Laschet[1], **M. Abouridouane**[2], **M. Fernández**[1], **M. Budnitzki**[1], **T. Bergs**[2]

[1]ACCESS e.V., RWTH Aachen University, Intzestraße 5, D-52072 Aachen, Germany
(g.laschet, m.fernandez, m.budnitzki)@access-technology.de
[2]Laboratory of Machine Tools and Production Engineering, RWTH Aachen University, Campus Boulevard 30, D-52074 Aachen, (m.abouridouane, t.bergs)@wzl.rwth-aachen.de

ABSTRACT

A multiscale approach is presented here to investigate the effect of the ferrite-pearlite microstructure after annealing on the subsequent machining process of steel gears. The case-hardening steel 18CrNiMo7-6 and a cost efficient alternative with reduced Cr and Ni content have been studied. After detailed microstructure characterization, three different scales are defined: the nano-scale with pearlite, built of ferrite-cementite bi-lamellas, the micro-scale, which corresponds to a RVE of the ferrite/pearlite microstructure and the macro-scale. In order to derive the effective flow behaviour of pearlite, virtual uniaxial tensile and shear tests of the ferrite/cementite bi-lamella are performed at the nanoscale. The flow behaviour of the ferrite phase is described there by an extension of the Kocks-Mecking law suitable for large machining strains. Moreover, at the nanoscale, the effective flow curve of the ferrite matrix having either small MnS or NbC inclusions is determined. At the microscale, effective flow curves for both steel grades are derived from virtual tests on 3D RVE's of both steel microstructures and compared with experimental measurements.

Keywords: Micromechanics, Homogenization, ferrite-pearlite microstructure, work hardening modelling, large plastic deformation.

1. Introduction

The worldwide demand of alternative energy production has strongly increased over the past decades. This demand requires among others the development of efficient wind energy converters. For this purpose, hot-forged steel gear wheels are widely used. Their manufacturing process chain involves various process steps such as continuous casting, hot rod rolling and forging. They are followed by a direct annealing to produce a ferrite-pearlite microstructure suitable for machining the gear preform. After machining, the carburising step allows to increase the wear resistance of the gears by inducing a martensite transformation at their surface.

In this study, two different steel grades are used to manufacture gear preforms: the case hardening 18CrNiMo7-6 alloy, commonly used in automotive gears, and a lower cost variant. Indeed, in order to reduce the production costs and increase its performance, a variant, named "substitute", has been developed recently by removing the expensive Ni, reducing Cr and adding Mn and Mo [1]. In order to investigate the impact of their chemistry and their specific ferrite-pearlite microstructure after annealing on the subsequent cutting process step, predictive micro-models have to be established and integrated into a comprehensive virtual simulation platform, like AixViPMaP [2]. Such an ICME approach [3] allows for the consideration of all relevant phenomena at the micro

scale within the macro-simulations of the gear production and constitutes a serious advantage over the studies describing the material behaviour only during a single production step.

The aim of the present multi-scale analysis is to derive macroscopic stress-strain curves for each gear preform based on the knowledge of its chemical composition and its ferrite-pearlite microstructure, building thus a valuable basis in order to answer following questions: 1. “How does the microstructure after annealing of each steel grade influence the subsequent machining step? 2. Is the cheaper variant a viable alternative to the 18CrNiMo7-6 alloy concerning its machinability?” in the 2nd part of the present paper. Experimental characterization of both steel grades, outlined in section 2, determines their microstructural features (grain size, interlamellar spacing and pearlite content) and identifies the nature, size and shape of the inclusions in the ferrite matrix. As pearlite is an eutectoid phase mixture, composed of alternating ferrite and cementite lamellae, three different scales have been distinguished for the ferrite-pearlite steel gear grades: the *nanoscale* where the pearlite is modelled by a repetition of ferrite/cementite bi-lamellas and the inclusions are modelled within the ferrite matrix, *the microscale* of the ferrite-pearlite microstructure and the *macroscale* of the cutting process. A two-level homogenization scheme is adopted here. It has been applied in the past with success to the derivation of anisotropic flow curves of a ferrite-pearlite pipeline steel [4] and gear steels [5]. In these investigations the work hardening model of Gutierrez and Altuna [6] was adopted for the ferrite phase. This model works well at small strains where the assumption of strain independence of the mean free dislocation path is valid. But, as very large strains occur in cutting operations, it is important to derive another physically based hardening law for the ferrite matrix and for ferrite in pearlite which takes strong dislocation interactions at large strains into account. The development of such model will be outlined in section 3.

Several physics-based models [7-14] have been developed based on the Kocks-Mecking-Estrin theory (KME) [7, 8], which describes the fundamental relationship between flow stress, work hardening and dislocation density evolution during plastic deformation. They formulate the rate of change of the dislocation density as a competition between storage and annihilation rates of dislocations during plastic deformation. Sinclair et al. [9] included the grain size effect on the initial work hardening behaviour by taking dislocation – grain boundary (GB) interactions into account. Moreover, the pile-up of dislocations at the GB induces a long-range back stress, responsible for a kinematic hardening contribution. Bouquerel et al [10] proposed to incorporate the influence of dislocation-dislocation interactions. Delincé et al [11] generalize Sinclair et al. model by limiting grain boundary dislocations (GBD) at large strains. Their model constitutes an interesting basis for our model description as several dislocation evolution mechanisms are well addressed. However, the experimentally observed nonlinearity of the decrease of the stress-strain slope with increasing stress at large strains is not addressed there. Therefore, we will extend Delincé’s model by introducing the Hariharan and Barlat [12] KME extension, namely the nonlinear dependence of the free dislocation path (D) on the dislocation density. Note that Bouaziz [13] and Barlat [14] proposed analogous KME model extensions to avoid too rapid saturation of strain hardening at higher stresses.

As already shown in [4], the anisotropic, inelastic behaviour of the cementite phase has also to be addressed in the bi-lamella homogenization of the pearlite. The delicate derivation of elastic and

inelastic properties of this metastable phase has been revisited, as outlined in section 4. Note that Berisha et al [15] performed a microscopic modelling of pearlite hardening and failure behaviour. However, they consider the cementite layer as isotropic elasto-plastic material and thus neglect their strong orthorhombic anisotropy. They describe ferrite by a phenomenological crystal plasticity law and used the spectral solver of DAMASK [16] to model strain localization at the grain level.

In section 5, the effective anisotropic elastic behaviour and flow curves of the ferrite/pearlite bi-lamella are derived as well as the equivalent elastoplastic behaviour of the ferrite matrix doted either with small, soft MnS particles (18CrNiMo7-6 grade) or with small hard NbC particles (substitute grade). Eventually, in section 6, effective flow curves of the ferrite-pearlite microstructures are derived and compared with experimental stress-strain curves for each steel grade. Moreover, the back- stresses in both ferrite-pearlite microstructures, induced by kinematic hardening, are determined based on the Allain-Bouaziz approach [17] and discussed there.

2. Experimental investigation: materials characterization and compression tests

2.1 Microstructure characterization

The chemical composition of the investigated steel grades is given in Table 1. The 18CrNiMo7-6 case hardening steel was produced by continuous casting in industry while the substitute grade was cast at the Institute for Ferrous Metallurgy (IEHK) of Aachen University. As detailed in [1], this Ni free variant has lower Cr content but increased Mn, Mo and C content.

Table 1. Chemical composition in wt % of the reference 18CrNiMo7-6 and of the substitute grade.

Steel	C	Cr	Ni	Mo	Mn	Nb	Al	Cu	Si	P
Ref.	0.18	1.55	1.6	0.27	0.5	0.03	0.03	0.30	0.24	0.015
Subst.	0.21	1.3	0	0.5	1.5	0.07	0.03	0.25	0.24	0.01

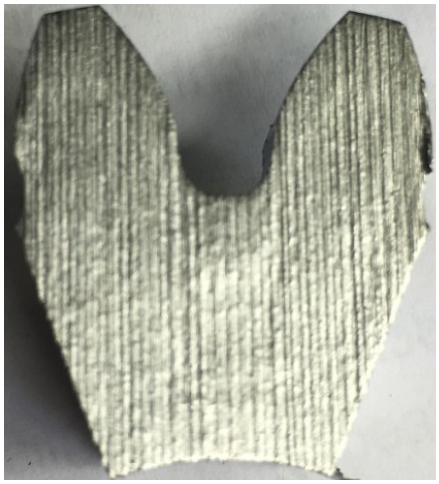

Fig. 1: Analysed tooth region of the gear preform.

As expected, the Electron Probe Micro-Analyses (EPMA) showed a ferrite-pearlite microstructure in the tooth region of both steel gear preforms after the annealing step (see Fig. 1 and 2). Note that this study investigates mainly the strongly stressed tooth region; whereas in Ref. [5] the bulk region of the gear was investigated. The lamellas of ferrite and cementite in the pearlite of the substitute grade are not so parallel and exhibit some wrinkles (see Fig. 2d); whereas the pearlite of the reference steel presents quasi-parallel lamellas (see Fig. 2b).

This has a direct impact on the definition of the lamella length and width. The EPMA images of the ferrite matrix show that small MnS inclusions exist in the 18CrNiMo7-6 alloy (see Fig. 3a);

whereas in the substitute steel small hard NbC carbides and few large CeS inclusions are detected in its ferrite matrix (Fig. 3b and 3c). The nature of the foreign phases in both ferrite matrices have been identified by using the Wavelength Dispersive X-ray Spectroscopy (WDS) technique. Using the image software AZtec, the number of inclusions, their shape and area are measured in microstructure windows of 1 mm^2 size within the zone of interest (see Fig.1). The pearlite contents, given in Table 2, correspond to the local value at the same tooth location in both preforms. In the reference grade, 8495 small MnS particles with an ellipsoidal shape were counted. They have a mean size of 0.132 μm^2. In the substitute steel 1474 small NbC carbides of ellipsoidal or prismatic shape having a mean size of 0.216 μm^2 and 198 large, quasi-spherical CeS inclusions with a mean size of 37.45 μm^2 were detected. The mean size of ferrite and pearlite grains is outlined in Table 3 for both steel variants. The lamella spacing and its extension are given also in Table 3. The mean length of the straight 18CrNiMo7-6 lamellas (see Fig. 2b) is easily identified to be 7 μm. However, the length of the curved lamellas in the substitute grade material is delicate to specify. Here, a width and length of 4.5 μm is adopted.

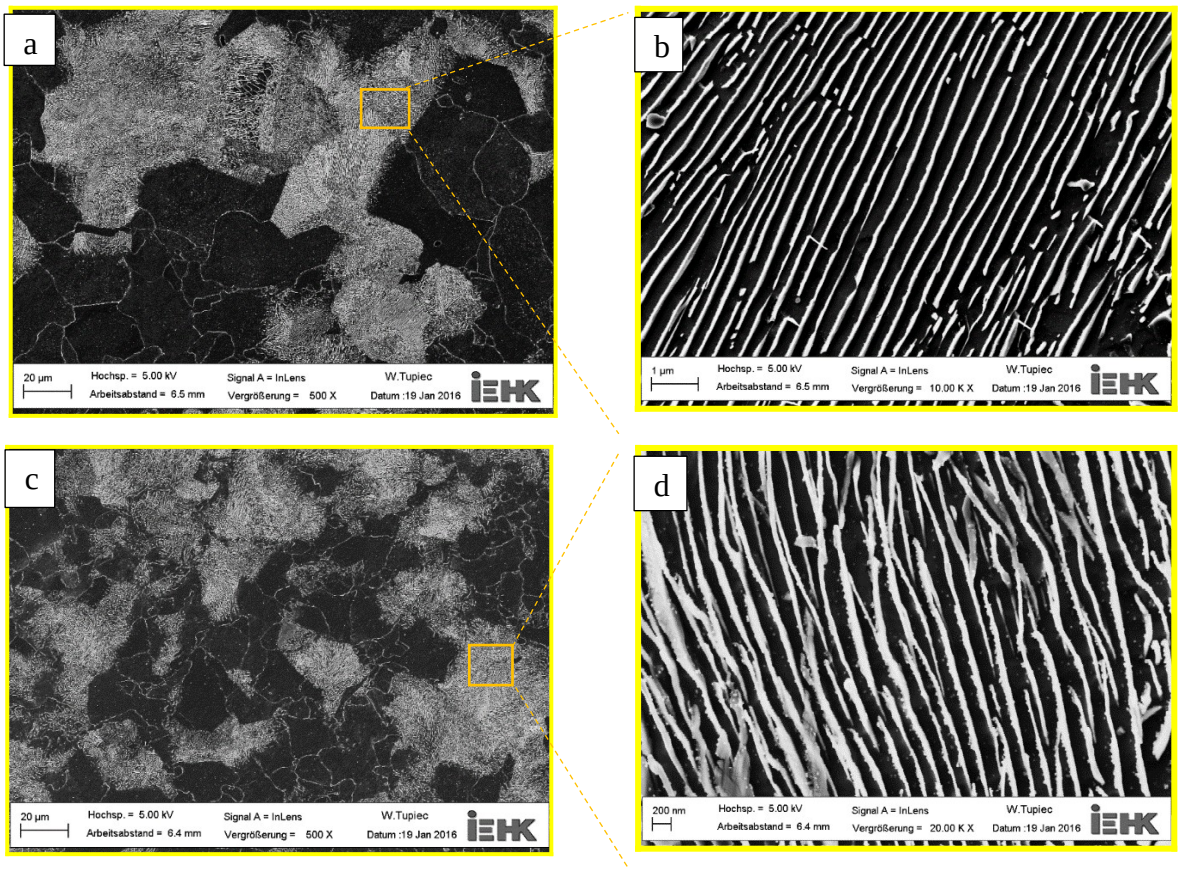

Fig. 2: EPMA analyses of the annealed 18CrNiMo7-6 steel a) and of the substitute variant c) in the tooth gear region of the gear and zoom of pearlite grain of reference b) and substitute variants d).

Compared to the 18CrNiMo7-6 steel, the substitute variant presents smaller grain sizes, a noticeable increase of pearlite content and a smaller interlamellar spacing, which induce stronger hardening.

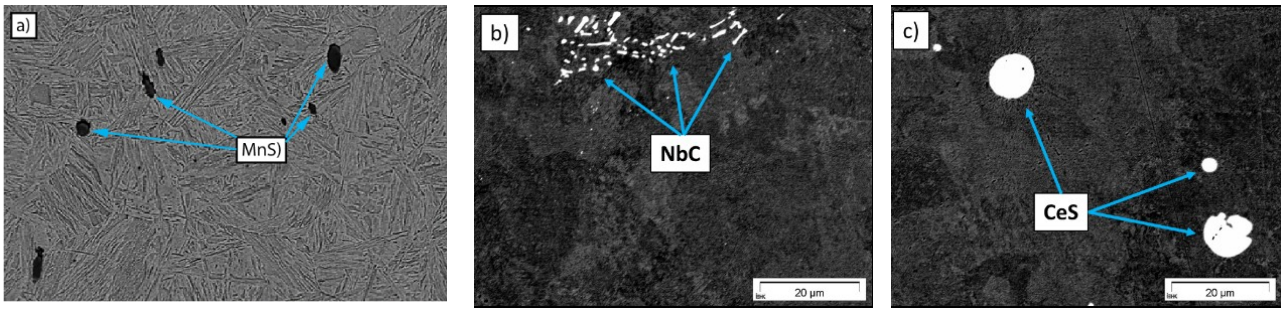

Fig. 3: EPMA images of the ferrite matrix of the 18CrNiMo7-6 steel a) and of the annealed substitute grade b); c) shows the detected inclusions in the substitute grade.

Table 2. Phase content in wt % of both grades in the tooth region of the gear preform and the area fraction (A_f in %) of the detected inclusions.

Grade	**Ferrite [%]**	**Pearlite [%]**	**Inclusions [%]**		
			MnS	**NbC**	**CeS**
Ref.	57	43	0.131	-	-
Subst.	46	54	-	0.021	0.322

Table 3. Average grain size, interlamellar spacing, length and width of the lamella in [µm] of both microstructures.

Grade	**Grain size [µm]**	**Interlamellar spacing [µm]**	**Lamellar length [µm]**
Ref.	31.16	0.3061	7.0
Subst.	16.51	0.2812	4.5

2.2 Compression test setup and results

To validate the flow curves determined by homogenization, compression tests were performed on a servo-hydraulic press using cylindrical samples with a high of 9 mm and a diameter of 6 mm, extracted from the tooth region of both gear preform variants. The samples were compressed in a single hit using either a very low strain rate of 2.5E-04 s^{-1}, corresponding to a quasi-static loading, or a strain rate of $\dot{\epsilon} = 0.01$ s^{-1} to a maximum deformation of $\varepsilon \approx 0.75$. Two samples per strain rate and steel grade have been compressed. To reduce the influence of friction Teflon was used as lubricant.

Subsequently, main elastoplastic flow

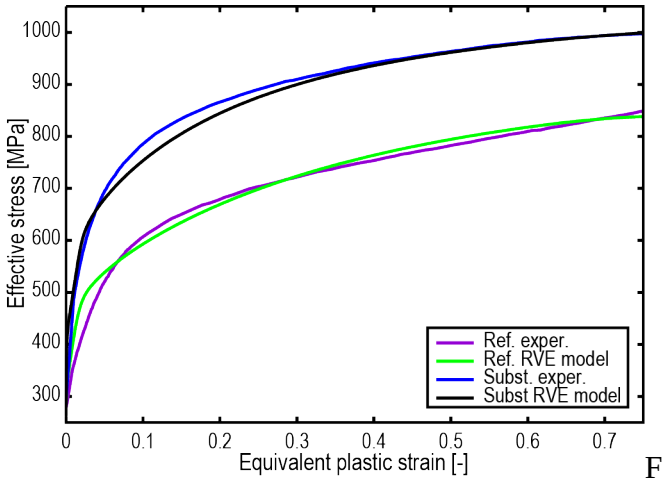

Fig. 4: Experimental flow curves at strain rate $\dot{\epsilon} =$¿ 2.5 10^{-4} s^{-1} and $\dot{\epsilon} =$¿ 0.01 s^{-1} derived from uniaxial compression tests.

curves were determined from the measured force-displacement data. In this process, the elastic deformation as well as settlements in the machine were compensated. The resulting mean flow curves are shown in Fig. 4. As expected, the substitute grade exhibits a stronger initial strain hardening than the 18CrniMo7-6 alloy due to smaller grain size and larger pearlite content. Higher strain rate ($\dot{\epsilon} = 0.01$ s^{-1}) induces a further slight increase of the work hardening of both steel grades.

3. Work-hardening model

First, the flow stress of work-hardened polycrystals is defined by the internal stresses due to the presence of forest and mobile dislocations. According to Taylor's theory [18], a general equation relates the macroscopic flow stress to the total dislocation density ρ via expression:

$$\sigma = \sigma_0 + \sigma_\epsilon = \sigma_0 + \alpha M b G \sqrt{\rho} \quad (1)$$

in which σ_0 is a strain and dislocation independent term, α is a numerical factor that characterizes the dislocation-dislocation interaction (α= 0.33), G the shear modulus and b the Burgers vector of the considered bcc ferrite phase and M is the Taylor factor. The second term of relation (1) specifies the isotropic hardening of the material. The initial yield strength σ_0 depends on the Peierls-Nabarro force and on the effect of solutes and it includes the grain size effect, well known as the Hall-Patch effect [19]. Hence, σ_0 can be written as:

$$\sigma_0 = \sigma_{00} + \sigma_{HP} = \sigma_{00} + \frac{k_{HP}}{\sqrt{D}} \quad (2)$$

in which k_{HP} is a material constant: $k_{HP} \cong 15\, MPa\sqrt{mm}$, D represents the average mean free path for dislocation movement and σ_{00} is the contribution of the Peierls force and solute solution strengthening. In the case of the ferrite matrix, D corresponds to the mean grain size; whereas for the ferrite layer within pearlite nearby to its thickness. According to Gutierrez & Altuna [6], the initial yield stress contribution σ_{00} can be expressed in function of the different solute elements in the considered steel grade:

$$\sigma_{00} = \sigma_{fr} + 32\,Mn + 678\,P + 83\,Si + 39\,Cu + 45\ni - 31\,Cr + 11\,Mo + 5544\left(N_{SS} + C_{SS}\right) \quad (3)$$

where σ_{fr} denotes the lattice friction, given by σ_{fr} = 77 MPa and the concentrations are expressed in wt%. N_{SS} and C_{SS} are respectively the interstitial atoms N and C in solid solution in the ferrite phase.

Second, according to Kocks, Mecking and Estrin's pioneer work [7, 8], the evolution of the total dislocation density with strain is a result of the competition between the production rate of dislocations and their annihilation rate due to dynamic recovery, which is temperature and strain rate dependent:

$$\frac{d\rho}{d\epsilon^p} = M\left(\frac{k_1\sqrt{\rho}}{b} - k_2\rho\right), \tag{4}$$

where k_1 is a material dependent storage constant and k_2 is the dynamic recovery constant and ϵ^p, the equivalent plastic strain.

In order to take the dislocation pile-ups at the grain boundaries into account, Delincé et al [11] generalized the original KME model (4): Grain Boundary Dislocations (GBD) increase the dislocation storage and produce also a net back stress (kinematic hardening effect). In their approach, GBD's cannot exceed a critical density and therefore their number saturates at large strains. They added an additional storage term due to the GBD density to the KME evolution law (4):

$$\frac{d\rho}{d\epsilon^p} = M\left(\frac{k_1\sqrt{\rho}}{b} - k_2\rho + \frac{k_3}{bD}\left(1 - \frac{\lambda^{\prime}}{\lambda}\right)\right), \tag{5}$$

in which $1/\lambda$ is the GBD line length per area surface of a grain boundary, $1/\lambda^*$ is interpreted as the maximum density of sites that can accept a GBD and $\left(1-\frac{\lambda^{\prime}}{\lambda}\right)$ expresses the proportion of „free sites" for an extra GBD. Furthermore, the GBD mean spacing is expressed by:

$$\frac{1}{\lambda} = \frac{1}{\lambda^{\prime}}\left[1 - \exp\left(\frac{-\lambda^{\prime} M\epsilon^p}{b}\right)\right]. \tag{6}$$

Introducing relation (6) in the differential equation (5), leads to:

$$\frac{d\rho}{d\epsilon^p} = M\left(\frac{k_1\sqrt{\rho}}{b} - k_2\rho + \frac{k_3}{bD}\exp\left(\frac{-M\lambda^{\prime}}{b}\epsilon^p\right)\right). \tag{7}$$

Third, dislocations which accumulate along a GB produce also kinematic hardening and cause a back stress *X* due to their polarization. Delincé et al [11] evaluated this back stress in presence or not of screening of the long range dislocation stress field by following expression:

$$X = \frac{M'}{2\pi}.\frac{Gb}{\lambda}\left[1 - \left(1 - \frac{w}{D}\right)\frac{\lambda^{\prime}}{\lambda}\right], \tag{8}$$

where M' is a generalized Taylor factor which depends on the grain shape and crystallographic structure and w corresponds to the width of the GB.

Note that under radial loading, like in uniaxial tensile tests, isotropic and kinematic hardening are combined into an effective flow stress by summing up expressions (1) and (8):

$$\sigma = \sigma_0 + \alpha MbG\sqrt{\rho} + \frac{M'}{2\pi}.\frac{Gb}{\lambda}\left[1 - \left(1 - \frac{w}{D}\right)\frac{\lambda^{\prime}}{\lambda}\right]. \tag{9}$$

Fourth, expression (7) of the Delincé KME model neglects the fact that the slope of the stress-strain curve becomes nonlinear at larger strains [12-14]. As we want derive a physically based model

suitable for cutting simulations, where large strains occur, it is important to further extend the dislocation evolution law (7). As suggested by Hariharan and Barlat [12], the pure linear dependence of the first storage term with $\sqrt{\rho}$ can be replaced by an exponential expression as follows:

$$\frac{d\rho}{d\epsilon^p} = M\,\text{¿}, \qquad (10)$$

where ψ is a positive material parameter, which has to be fitted to experimental data.

Expression (10) is path independent and assures that the mean free dislocation path D decreases with the strain increase and that the stress-strain slope varies nonlinearly with the stress, as observed experimentally [20]. Expanding the exponential in series, ignoring the higher order terms and setting ψ= 1.0, we retrieve the original Delincé model. Relation (10) is an ODE that is solved numerically using a 4th order Runge-Kutta scheme, starting with a known or estimated initial dislocation density ρ_0. The obtained total dislocation density is then introduced in equation (9) to get the equivalent flow stress.

Eventually, in Table 4 are summarized all the material parameters of the developed micro-mechanical work hardening model (eq. 9 -10).

Table 4: Description, symbol, value and unit of the different parameters of the micro-mechanical model.

Parameter	**Symbol**	**Value**	**Unit**
Shear modulus of ferrite	G	80.	GPa
Magnitude of Burgers vector	B	$2.5\ 10^{-10}$	m
Taylor constant	α	0.33	-
Taylor factor	M	3	-
Dislocation mean free path	D	location dependent	m
Carbon content in ferrite	C_{SS}	grade dependent	wt.%
Minimal GBD spacing	λ^*	$2.\ 10^{-8}$	m
Screening parameter	W	5.10^{-7}	m
Dislocation storage constant	k_1	grade dependent	-
Dislocation annihilation constant	k_2	grade dependent	-
GBD storage term	k_3	0.1	-
Nonlinear hardening coefficient	ψ	grade dependent	M
Back-stress factor	M'/M	0.4	-
Lattice friction stress	σ_{fr}	77	MPa
Hall-Petch coefficient	k_{HP}	15.	MPa.$\sqrt{mm}$
Initial dislocation density	ρ_0	location dependent	m^{-2}

4. Micromechanical modelling of ferrite and cementite

4.1 Elastic behaviour of ferrite and cementite

Based on the chemical composition of each steel grade (see table 1), the Ghosh and Olson approach [21] is used to evaluate a concentration dependent shear modulus of the single crystal ferrite phase at room temperature. Then, by assuming the same stiffness ratios C_{11}/C_{44} and C_{12}/C_{44} as for Fe0.023C0.17Mn ferrite single crystal [22], we get the cubic elastic constants of the ferrite phase at room temperature as shown in Table 5.

Table 5: The cubic elastic constants of the ferrite phase at room temperature.

Grade	**C_{11} [GPa]**	**C_{12} [GPa]**	**C_{44} [GPa]**
ref.	227.6	131.3	115.1
subst.	229.2	132.2	115.9

The cementite phase of the eutectoid pearlite has an orthorhombic lattice (a = 5.09 A, b = 6.74 A, c = 4.52 A). This phase is substantially harder than ferrite and quite brittle. As cementite is metastable at all temperatures, it is difficult to produce test specimens for mechanical testing. Therefore, first principles simulations are performed to derive the elastic constants of cementite. Mauger et al. [23] derived recently via constant volume DFT simulations firstly temperature dependent elastic constants of cementite. These theoretical values overestimate however experimentally measured Young moduli at RT by Koo et al [24] and Alkorta and Gil Sevillano [25]. Applying Koo's reduction factor 8.6%, to Mauger's elastic constants at RT we obtain the elastic constants of cementite at table 6. These elastic constants underlie *the pronounced elastic anisotropy of the cementite phase*, characterized by a very small shear stiffness C_{44}. Note that these elastic constants improve Jiang et al.'s [26] ones, obtained at 0 K and used in our previous investigations [4, 5], by reducing the global cementite stiffness and its extreme shear anisotropy.

Table 6: Elastic constants of cementite at room temperature [GPa].

C_{11}	**C_{22}**	**C_{33}**	**C_{12}**	**C_{13}**	**C_{23}**	**C_{44}**	**C_{55}**	**C_{66}**
314.8	306.4	280.1	130.7	123.8	157.2	28.8	120.4	121.3

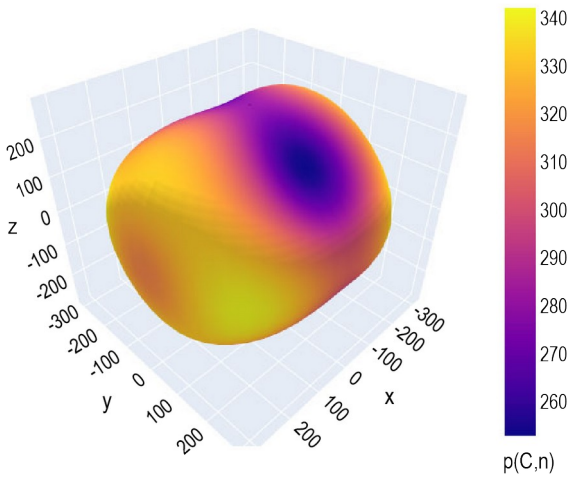

The orthorhombic symmetry of its Hooke tensor *C* is illustrated via the normal projections p(C,n) of the Hooke matrix in Fig. 5. The normal projection of tensor *C* on normal vector *n* is defined by:

$$p(C,n) = \sum_{i,j,k,l=1}^{3} C_{ijkl} n_i n_j n_k n_l \qquad (11)$$

Note that each point of the depicted surface corresponds to the considered normal multiplied by *p(C,n)*.

As both investigated steel grades are hypo-eutectoid

Fig. 5: Normal projection p(*C,n*) [GPa] of Hooke tensor *C* of cementite.

steels, the orientation relationship of Isaichev [27] between ferrite and cementite is adopted here for both steel grades.

4.2 ***Elastoplastic behaviour of ferrite***

4.2.1 Ferrite matrix

The generalized KME law (10) was used to describe the evolution of the total dislocation density during plastic deformation in the ferrite matrix. The corresponding macroscopic flow stress σ is given by expression (9). The different chemical composition of both investigated steel grades enters via expression (3) in the definition of the initial yield stress contribution σ_{00}. As the carbon solution in ferrite is multiplied by a large factor, its value is the dominant term, which is difficult to specify as the annealed microstructure is not in thermodynamic equilibrium. We adopt here C_{SS} = 0.003 wt% for the 18CrNiMo7-6 grade and a slightly higher value C_{SS} = 0.004 wt% for the substitute, due to the higher carbon content in its composition (see Table 1). Moreover, the initial dislocation density after annealing is assumed to be low in both steels: $\rho_0 = 2.\ 10^{12}$ m^{-2}. The mean grain size in both grades specifies their specific mean free path: D=31.16 μm for reference steel and D=16.51 μm for the substitute. The parameters of the isotropic and kinematic contributions (eq. 7 and 8) of the GBD are defined according to Delincé et al [11]: M' = 0.4M, minimal GBD spacing λ^* = 0.02 μm, screening width w = 0.4 μm and coefficient k_3 = 0.1.

A sensitivity analysis of the generalized KME law (10) is performed by varying the most sensitive parameters, namely the storage constant k_1, the dynamic recovery k_2 and the hardening coefficient ψ. In figure 6 are drawn the sensitivities of parameters k_1 and k_2 and in Fig. 7.left the sensitivity of hardening parameter ψ. As expected, the variation of the storage constant k_1 increases significantly the yield stress, mainly at small strains; whereas the dynamic recovery k_2 reduces it. Note that the nonlinear hardening parameter ψ has the largest impact on the yield stress. Due to this strong impact, its variation range is restricted here closely to the value identified by Hariharan & Barlat [12]: $0.055 \leq \psi \leq 0.065$ [μm]. Then, the unknown KME model parameters k_1 and k_2 of the ferrite matrix are derived from a least-square fitting of the effective flow obtained by the two-level homogenization with the experimental quasi-static flow curve ($\dot{\epsilon} =$¿ 2.5 10^{-4} s^{-1}) (see Fig. 4).

In table 7 are reported their values for both steel grades. In Fig. 8.left are drawn the corresponding elastoplastic flow curves of the ferrite matrix for the studied gear steels. As expected, the substitute alloy presents stronger hardening of its matrix than the reference grade due to the smaller grain size. A noticeable larger storage coefficient k_1 characterizes this behaviour. On the other side, its larger recovery coefficient k_2 induces lower yield increase at larger strains.

Table 7: Fitted parameters of the generalized KME law for the ferrite matrix of both steel grades.

Grade	**k_1**	**k_2**	**ψ** [μm]
Reference	0.150	1.05	0.06
Substitute	0.242	1.70	0.055

4.2.2 Ferrite in pearlite

The main differences between ferrite in the matrix and in the pearlite eutectoid are the different mean free dislocation path D of the ferrite in pearlite and the absence of screening for the GBDs. The residual dislocation density after annealing is assumed to be slightly larger there than in the matrix: ρ_0 = 3. 10^{12} m^{-2}. At thermodynamic equilibrium, the volume fractions of cementite and ferrite in pearlite are V_C =1/9 and V_F = 8/9. Thus, the ferrite layer thickness λ_F is easily given by: λ_F = 8/9.λ.

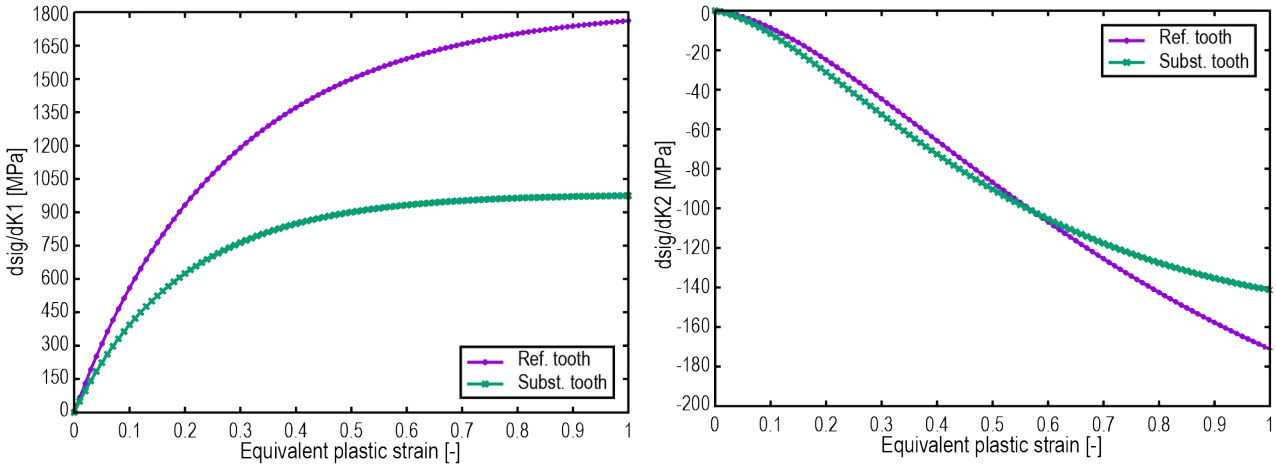

Fig. 6: Sensitivity of the generalized KME yield stress of the ferrite matrix of both steel grades with respect to the storage constant k_1 (left) and to the recovery parameter k_2 (right).

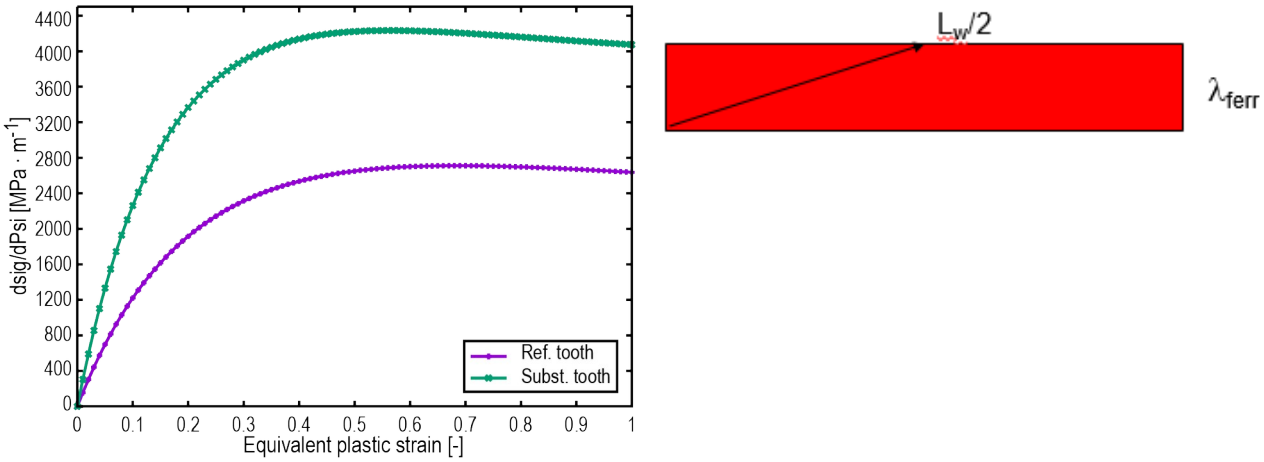

Fig. 7: Sensitivity of the generalized KME yield stress of the ferrite matrix of both steel grades with respect to the nonlinear hardening parameter ψ (left). 2D definition of dislocation mean free path D for ferrite in pearlite (right).

In a first approximation, the mean free path D of ferrite can be expressed via expression (12) (see Fig. 7.right), where L_w is the width and L_e the extension of the layer:

$$D = \sqrt{\square_F^2 + \left(L \text{¿¿} w^2 + L_e^2\right)/4 \text{¿}} \qquad (12)$$

With the interlamellar spacing, width and extension given in table 3 for both grades, the mean free path becomes $D_{f,Ref} = 4.957$ μm for the 18CrNiMo7-6 alloy and $D_{f,Sub} = 3.192$ μm for substitute grade respectively. Performing then an analogous sensitivity analysis for the ferrite in pearlite described by the KME model (10) as for the ferrite matrix, followed by a least-square fitting via the only available experimental stress-strain curve (see Fig. 4), we obtain the fitted material parameters k_1, k_2 and ψ of table 8 for ferrite in pearlite.

Table 8: Fitted parameters of the generalized KME law for the ferrite layer in pearlite of both steel grades.

Grade	$\mathbf{k_1}$	$\mathbf{k_2}$	ψ [μm]
Reference	0.235	1.06	0.06
Substitute	0.365	2.20	0.06

Compared to the ferrite matrix the storage constant k_1 has increased substantially by 56.7% for the reference alloy and by 50.38 % for the substitute variant. The nonlinear hardening coefficient ψ is unchanged for the reference alloy and increases slightly for the substitute; whereas the dynamic recovery constant k_2 is quasi constant for the reference alloy and increases by 29.4% for the substitute. In Fig. 8.right are drawn, for both grades, the flow curves of the ferrite phase in pearlite. Again the flow curve of the substitute alloy presents larger hardening than the reference one mainly due to the reduced mean free dislocation path and interlamellar spacing. Moreover, the initial yield stress of substitute is higher due to the Hall-Petch effect induced by its smaller mean free dislocation path D.

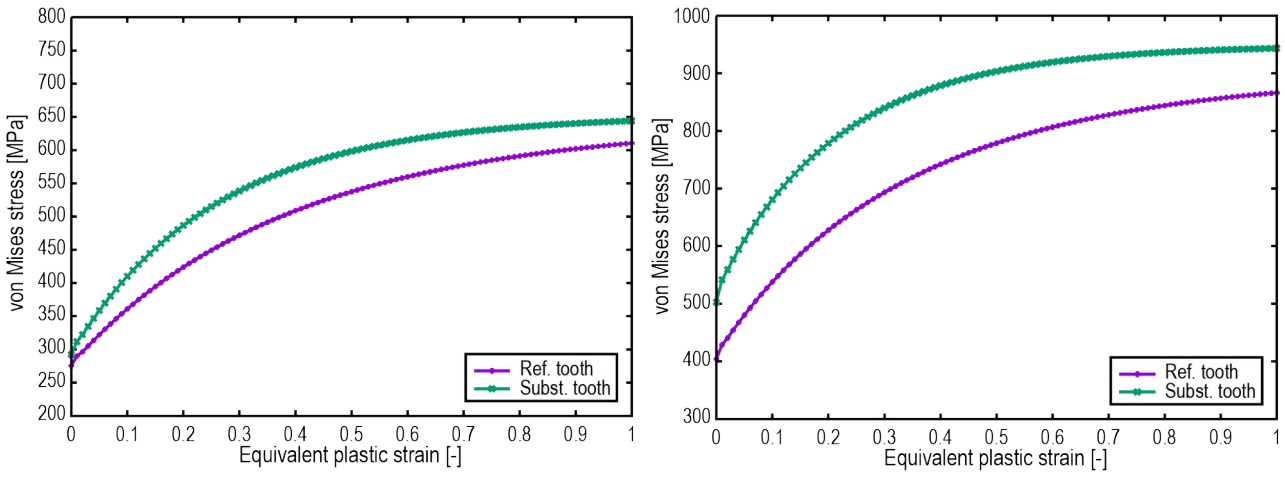

Fig. 8: Elastoplastic behaviour of ferrite matrix (left) and ferrite in pearlite (right) for both steel grades.

4.3 *Anisotropic inelastic behaviour of cementite*

As cementite is metastable at all temperatures, it is delicate to produce specimens for mechanical testing. Nonetheless, Luque et al. [28] deduced from indentation tests at RT on single

crystal cementite plates a mean strength of 4 GPa. Based on this yield strength value, Laschet et al. [4] have shown that it is important to take not only its inelastic behaviour but also its anisotropic nature into account. For the polycrystalline cementite lamella, we adopt again the anisotropic Hill yield criterion [29], where each tensile yield stress ratio R_{ii} ($R_{ij}=\frac{\sigma_{ij}^{Y}}{\sigma_0}$; with $\sigma_0=\sigma_{11}^{Y}$) is given by the corresponding stiffness ratio C_{ii}/C_{11} with i=2, 3. Then, the lowest compression strength of 2.76 GPa, measured by Umemoto et al. [30], is used here to specify the smallest yield ratio R_{23} in the shear plane 2-3; whereas in the planes 1-2 and 1-3 larger shear yield ratios are adopted, as larger experimental shear stiffnesses are measured in these planes [25]:

$$R_{11} = 1 \;;\; R_{22} = 0.97 \;;\; R_{33} = 0.89 \;;\; R_{12} = 0.78 \;;\; R_{13} = 0.77 \;;\; R_{23} = 0.69. \quad (13)$$

To derive a realistic estimate of the plastic behaviour of the cementite phase, the recent X-ray diffraction measurements by Taniyama et al. [31] of the dislocation density in the cementite layer of a drawn pearlitic steel at different strains are used here: $\rho_0 = 2.\ 10^{13}$ m^{-2} at $\varepsilon = 0.$; $\rho = 4.\ 10^{14}$ m^{-2} at $\varepsilon = 0.24$ and $4.7\ 10^{14}$ m^{-2} at $\varepsilon = 3.35$. These strain dependent densities are fitted here by a hardening law of Gutierrez-Altuna type [6]:

$$\rho=\frac{1}{bD\,k_2}\left[1-e^{\left(-k_2 M\epsilon\right)}\right]+\rho_0 e^{\left(-k_2 M\epsilon\right)}, \quad (14)$$

where D = 12 nm and b = 0.503 nm [31]; whereas parameter k_2 is unknown and fitted.

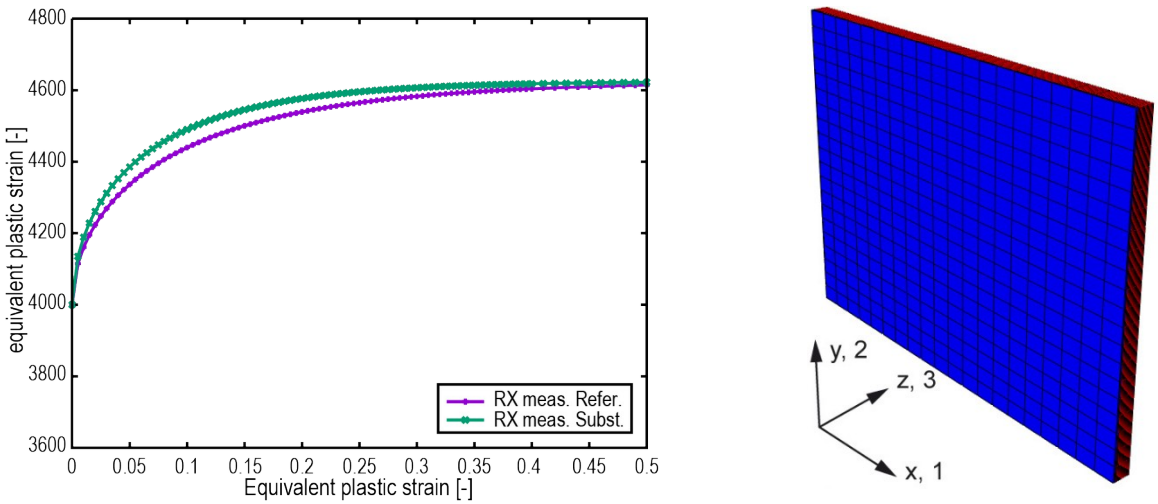

Fig. 9: Elasto-plastic curves of cementite in pearlite of reference and substitute steel grades, derived from RX measurements (left). Bi-lamella RVE discretization of pearlite (reference steel) and definition of the local axis system $\mathbf{e}_1$, $\mathbf{e}_2$, $\mathbf{e}_3$ (right).

Then, assuming that the pearlitic steel of Taniyama's analysis and the investigated gear steels have the same $\frac{1}{bDk_2}$ coefficient in expression (14), we get a different hardening behaviour of the cementite in both steels (see Fig. 9.left), as the mean free path D is different in their respective cementite layer: $D_{C,Ref}$ = 4.95 μm and $D_{C,sub}$ = 3.54 μm. Assuming very low initial dislocation density in cementite (ρ_0 = 1. 10^{12} m^{-2}), the fit process leads to k_2 = 2.285 (reference steel) and k_2 = 3.187 (substitute alloy), respectively. These hardening laws present at small strains a yield increase from 4 GPa up to 4.5 GPa, followed by a plateau at larger strains, as outlined in Fig. 9.left.

5. Nanoscale homogenisation

The characterization of both steel grades reveals that the size of the MnS inclusions (d = 0.132 μm^2) in the ferrite matrix of the reference steel and of the NbC inclusions (d = 0.216 μm^2) in the substitute matrix is an order of magnitude smaller than the mean size (d ≥ 17 μm^2) of ferrite or pearlite grains, while the larger CeS inclusions in the substitute grade are of the same magnitude. Therefore, a three-level homogenization scheme is adopted, where at the lowest scale (nano) a) the pearlite bi-lamella formed of ferrite and cementite, b) the 18CrNiMo7-6 ferrite matrix, containing MnS particles, and c) the substitute ferrite matrix, dotted with small NbC carbides, are homogenized separately.

5.1. Effective mechanical properties of pearlite in both steel grades

5.1.1 Effective elastic properties of pearlite

The geometry of the bi-lamella RVE's is shown in Fig. 9.right. The thickness, width and length of these bi-lamella pearlite RVE's are outlined in table 3. Both simple RVE's are meshed with 7200 linear hexahedral elements and 3D periodic boundary conditions are applied. Adopting the Isaichev orientation relationship between the cementite and ferrite phases, the 1st order asymptotic homogenization with HOMAT v6.0 [32] provides following Hooke matrix (in GPa) of the pearlite of the 18CrNiMo7-6 steel in the local axis system $\mathbf{e}_1$, $\mathbf{e}_2$, $\mathbf{e}_3$ of Fig 9.right (Voigt notation):

$$H_{ref}^{eff} = \begin{vmatrix} 310.65 & 91.23 & 96.45 & -10.13 & -10.12 & 7.19 \\ 91.23 & 304.64 & 104.56 & 2.10 & 14.41 & 16.27 \\ 96.45 & 104.56 & 297.68 & 8.26 & -4.41 & -24.14 \\ -10.13 & 2.10 & 8.26 & 66.74 & -20.58 & 11.20 \\ -10.12 & 14.41 & -4.41 & -20.58 & 77.10 & -11.46 \\ 7.19 & 16.27 & -24.14 & 11.20 & -11.46 & 75.02 \end{vmatrix} \quad (15)$$

This result is meaningful: pearlite exhibits *an anisotropic elastic behaviour with extension-shear coupling*, due to the rotation of the cubic properties of the ferrite lamella in the cementite axis system. From this Hooke matrix and the analogous one for the substitute pearlite, effective orthotropic engineering constants (in GPa) and their mean values are derived in the local cementite axis system and reported in table 9. Fig. 10 shows the normal projections of the effective Hooke matrix of pearlite. This representation emphasises that pearlite has a quasi-cubic anisotropy due to the large influence of the cubic ferrite layer.

Table 9: Effective orthotropic and mean Young and shear modules [GPa] for both steel grades.

Steel	E_1	E_2	E_3	E_m	G_{12}	G_{13}	G_{23}	G_m
Ref.	259.63	243.48	230.53	244.55	66.93	67.69	58.94	64.52
Subst.	261.28	245.03	231.96	246.09	67.31	68.14	59.26	64.90

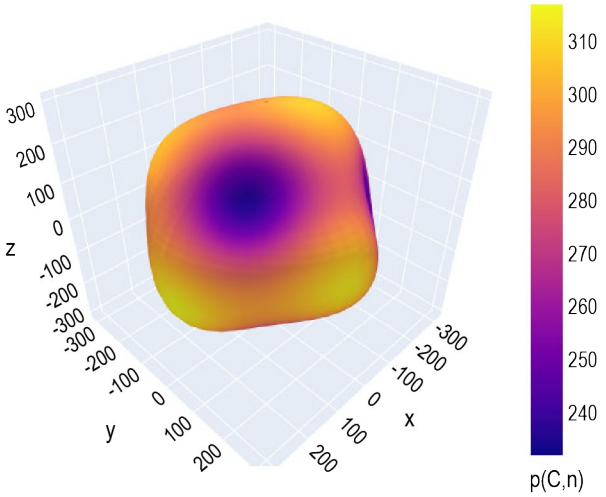

Fig. 10: Normal projections of the effective Hooke tensor of pearlite in the local axis system $\mathbf{e}_1$, $\mathbf{e}_2$, $\mathbf{e}_3$.

Independent of the steel grade, the Young's modulus in thickness direction E_3 is smaller than both in-plane moduli E_1 and E_2 with $\Delta E_{3\text{-m,ref}}$ = -5.73% and $\Delta E_{3\text{-m,sub}}$ = -5.74%, respectively. Its shear stiffness is more anisotropic with $G_{13} > G_{12} > G_{23}$: $\Delta G_{23\text{-m,ref}}$ = -8.64% ; $\Delta G_{23\text{-m,sub}}$ = -8.69%. However, due to the large presence of cubic ferrite this anisotropy is substantially less pronounced for pearlite than for the cementite layer: $\Delta G_{23\text{-m,ref}}$ =-68.06%.

5.1.2 Effective elasto-plastic behaviour of pearlite

In order to derive the effective elasto-plastic constitutive laws of the eutectic pearlite virtual uniaxial tensile and shear tests are performed on the same discretized bi-lamella for both steel grades. In Fig. 11.left the predicted effective elasto-plastic flow curves are drawn for the uniaxial tensile test in the in-plane $\mathbf{e}_1$ direction (Fig. 9.right). Independently of the pearlite design, both effective flow curves present a strong change in hardening when cementite begins also to yield. In fact, initial yielding occurs in the ferrite layer; whereas the cementite layer continues to deform elastically, leading to a strong stress increase at small strains. Compared to the 18CrNiMo7-6 grade, the substitute grade has a higher initial yield stress; whereas at large strains, its hardening increase is less pronounced. Note that the pearlite hardening is mainly governed by the response of ferrite.

The flow curves derived from the virtual uniaxial tensile and shear tests are reported on Fig. 11.right. The pearlite phase has *an orthotropic elasto-plastic behaviour*, where the in-plane flow curves ($\mathbf{e}_1$ and $\mathbf{e}_2$ directions) exhibit a stronger hardening than the flow curve in thickness direction $\mathbf{e}_3$: $H_{xx} > H_{yy} > H_{zz}$. The in-plane shear test provides an equivalent flow curve with a slightly reduced hardening. However, this hardening is larger than the one deduced from the both out-plane shear tests. For each effective flow curve of both steel grades, local stress ratios are evaluated at selected plastic strains in the range [0. – 0.6] and then averaged. These main stress ratios are outlined in Table 10.

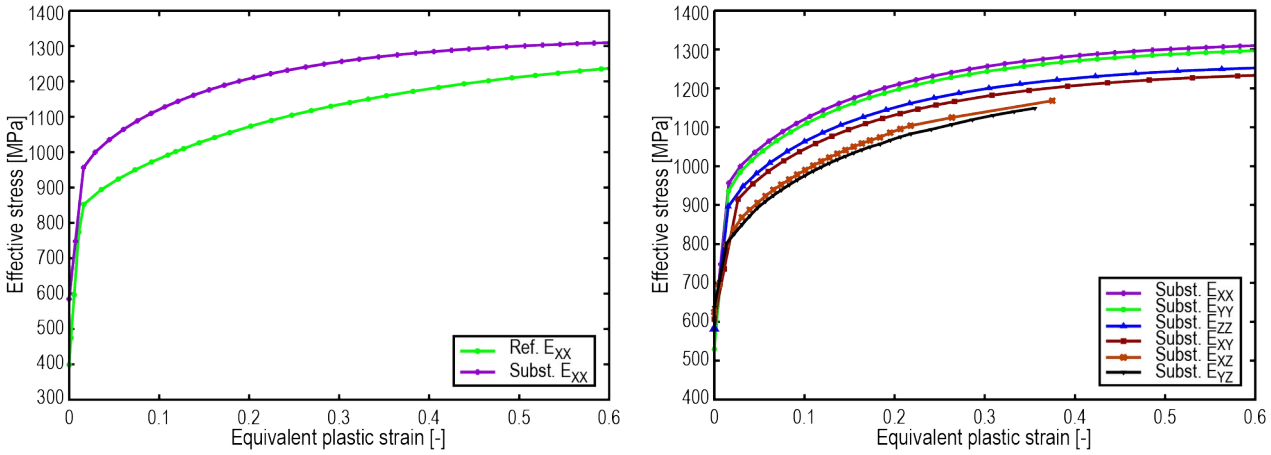

Figure 11: Effective elasto-plastic stress-strain curves of pearlite: reference uniaxial tensile curve for both steel grades (left); effective flow curves of substitute alloy derived from virtual uniaxial tensile and shear tests (right).

Table 10: Derived mean stress ratios ($R_{ij}=\frac{\sigma_{ij}^{Y}}{\sigma_0}$; with σ_{ij}^{Y} the measured yield stress and $\sigma_0=\sigma_{11}^{Y}$) of the pearlite eutectoid in both steel grades.

Steel	**R_{11}**	**R_{22}**	**R_{33}**	**R_{12}**	**R_{13}**	**R_{23}**
Reference	1.0	0.9846	0.9372	0.9345	0.8873	0.8820
Substitute	1.0	0.9878	0.9531	0.9340	0.9091	0.9053

These stress ratio results show that *the 18CrNiMo7-6 steel grade presents a stronger yield anisotropy than the substitute grade*. Mainly its out-plane shear stress ratios R_{13} and R_{23} are lower than the corresponding ratio of the substitute alloy.

5.2 ***Effective ferrite matrix of the 18rNiMo7-6 steel grade***

The observed MnS inclusions (see Fig. 3.a) in the ferrite matrix of the reference alloy are more compliant [33] and softer in plasticity [34] than the ferrite phase. At room temperature, their initial yield stress σ^{Y} is 88.2 MPa and at an equivalent plastic strain $\bar{\epsilon}^{pl}=0.2$, the equivalent stress reaches 130 MPa. The ferrite matrix is described, as outlined in Sec. 4.2.1, by a generalized KME hardening law (see Fig.8.left). A small RVE of 80 μm^3 extension is generated with the commercial program Digimat-FE [35]. 3D periodic boundary conditions are imposed at its outer surface. It contains 28 small MnS spheres, having a volume fraction of 0.03875% and 15 slightly larger ellipsoids (V_f = 0.09225%), which are randomly distributed within the RVE. Uniaxial virtual tensile test has been performed on the discretized RVE. In Fig. 12.left the effective flow curve of the ferrite matrix dotted with MnS particles, the pure ferrite flow curve and the elastoplastic behaviour of the MnS are plotted. Obviously the stiffness and hardening reduction of the effective ferrite matrix is marginal. The coefficients A, B and n of the Ludwik hardening law $\sigma=A+B\epsilon^{n}$, obtained by least-square fit, quantify this small hardening reduction of the 18CrNiMo7-6 ferrite matrix: Ferrite + MnS: A = 258.20 MPa, B = 414.19, n = 0.5562; pure Ferrite: A = 258.41 MPa, B = 414.58 MPa, n = 0.5564.

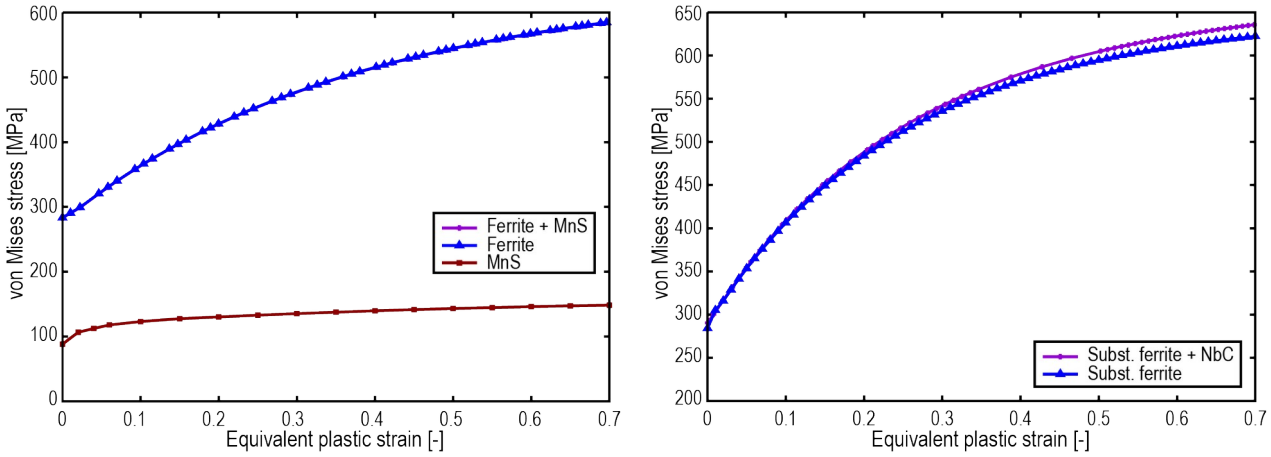

Figure 12: Elasto-plastic flow curves of the effective ferrite matrix of both steel grades: reference 18CrNiMo7-6 grade (left) and substitute grade (right). The flow curves of the corresponding pure ferrite matrix and of the MnS inclusions are also shown.

5.3 *Effective ferrite matrix of the substitute steel grade*

The NbC carbides are stiff inclusions in the ferrite matrix of the substitute grade. They are cubic with C_{11} = 557.3 GPa; C_{12} = 162.4 GPa; C_{44} = 146.5 GPa [36, 37], have a noticeable Zener anisotropy $A^z = \frac{2C_{44}}{(C_{11}-C_{12})} = 0.74$ and deform purely elastically in our simulation. The hardening behaviour of the ferrite phase of the substitute grade is again described by the generalized KME law (Eq. 10). A periodic RVE of extension 100 μm^3 is generated; it contains 9 randomly distributed ellipsoids and 4 prismatic inclusions with a total volume fraction of V_f = 0.0213%, corresponding to the experimental characterization. Virtual tensile tests are then performed on this RVE. In Fig. 12.right the deduced effective elastoplastic flow curve as well as the flow curve of the ferrite matrix of the substitute alloy are shown. From these curves the following Ludwig hardening coefficients are derived by least-square fit: pure ferrite matrix: A = 243.41 MPa, B = 466.08 MPa, n = 0.4254; effective matrix with NbC inclusions: A = 251.99 MPa, B = 469.12 MPa, n =0.4443. Even though the volume fraction of NbC carbides is small, the Ludwig hardening coefficients increases noticeably: the initial yield stress A by ΔA = 3.52% and hardening exponent n by Δn = 4.45%.

6. Modelling and homogenization of both steel grades at the microscale

6.1 *Model generation*

Representative Volume Elements (RVE) of extension 150 μm^3 are generated for both steel grades at the microscale. The pearlite content of each RVE varies accordingly to the experimental characterization (see Table 2): 43% in the reference RVE and 54% in the substitute one. A Laguerre tessellation is performed using Neper v3.5.1 [38] in order to generate ferrite-pearlite microstructures for each steel grade, with a log-normal grain size distribution, which respects their respective average grain size: 31.16 μm (ref.) and 16.51 μm (subst.) (see Fig. 13). As the CeS inclusions are

large (D_{CeS} = 37.45 μm) and of the same size as the ferrite grains, three ferrite grains are converted afterwards in CeS inclusions, in order to respect their volume fraction: V_{CeS} = 0.3217% in the substitute RVE. They deform elastically and have cubic symmetry [39] with C_{11} = 195.6 GPa, C_{12} = 26.51 GPa and C_{44} =75.595 GPa. In both RVE's the grains are randomly oriented. Neper uses Gmsh [40] to generate a tetrahedral volume mesh for both tessellations. Then, 3D periodic boundary conditions and imposed displacements are applied to perform uniaxial tensile virtual tests. The two-phase ref. model contains 986 grains, 365,960 linear tetrahedrons and 67,915 nodes; whereas the three-phase subst. model is built of 1432 grains, which are meshed by 613,021 linear tetrahedral elements and 116,184 nodes.

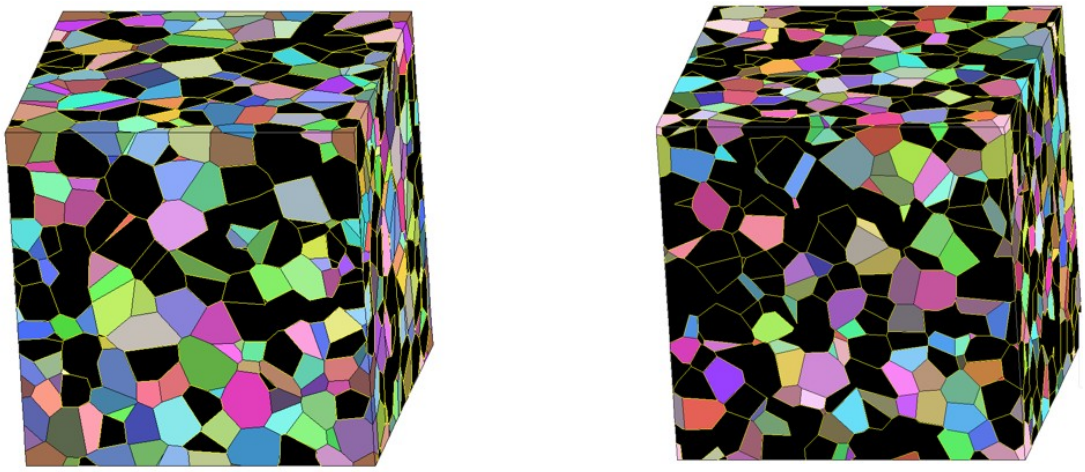

Figure 12: Generated RVE's: reference alloy (left); substitute steel (right). The coloured grains are ferrite ones; whereas the dark ones are effective pearlite grains.

6.2 Effective macroscopic stress-strain curves of both steel grades

Virtual uniaxial tests were performed with Abaqus Standard [41] for both specified RVE models in order to derive their respective effective macroscopic elasto-plastic behaviour at room temperature. Note that these macroscopic flow curves are obtained by volume averaging the micro-strains and -stresses of each virtual test by fulfilling the Hill-Mandel condition [42]. In Fig. 13, the predicted effective flow curve as well as the corresponding experimental one are depicted for both steel grades. Independent of the considered steel grade, both predicted flow curves exhibit a strong change in their hardening behaviour, when the pearlite grains begin also to yield. This occurs when the cementite and/or the cementite/ferrite boundary interlayer goes in an inelastic regime.

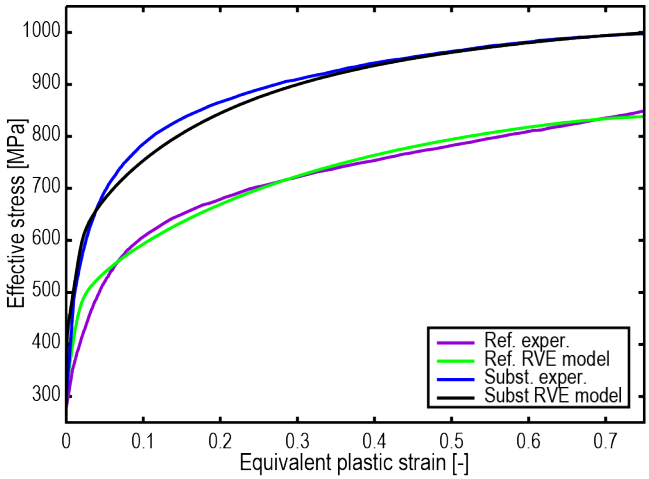

Figure 13: Predicted effective elastoplastic curves and the corresponding quasi-static experimental flow curves ($\dot{\epsilon} = 2.4\, s^{-1}$) of the reference and substitute steels.

Due to its higher pearlite content (54% vs. 43%) and its smaller mean grain size (17.2 μm vs. 29.0 μm) the substitute grade shows a stiffer equivalent hardening behaviour. For the reference alloy, the predicted flow curve exhibits stronger hardening than the corresponding experimental curve at small plastic strains (ε < 0.08); whereas for the substitute steel grade, the hardening increase of the RVE model underestimates slightly the hardness in the experiment one in the range [0.06 ≤ ε ≤ 0.27]. Overall, an excellent agreement of the hardening behaviour with the experimental one is observed for both steel grades at larger strains (ε > 0.3), which is the relevant range in the subsequent machining step.

6.3 Effective kinematic hardening behaviour of both steel grades

To complete the elastoplastic homogenization of the investigated ferrite-pearlite steel microstructures, their impact on the effective kinematic hardening behaviour of each steel grade is determined here. To perform this investigation, the rather simple model of Allain-Bouaziz [17] is adopted here to express the macroscopic internal stresses X in function of the equivalent plastic strain $\bar{\epsilon}^{pl}$. In their model, the total internal stress is the sum of two contributions: X' the internal stress due to deformation incompatibility between ferrite and pearlite (a mixing term) and X'' a contribution resulting from the intrinsic kinematic hardening of pearlite, which depends on its interlamellar spacing λ. The total internal stress X is given by expression (16):

$$X(\bar{\epsilon}^{pl}) = X' + X'' = (1 - f_{pearl}) f_{pearl} \Delta\sigma(\bar{\epsilon}^{pl}) + f_{pearl} \frac{A}{\sqrt{\square}} \left[1 - \exp^{(-Q\bar{\epsilon}^{pl})}\right] \qquad (16)$$

where f_{pearl} is the volume fraction of pearlite, $\Delta\sigma(\bar{\epsilon}^{pl})$ the yield stress difference between effective pearlite and ferrite, A and Q are material parameters, determined experimentally [17]: A= 0.185 MPa.$\sqrt{m}$ and Q = 185.

In Figure 14 are drawn the variation of the total internal stress X, the mixing contribution X' and the intrinsic pearlitic contribution X'' for the two investigated steel grades. Independent of the grade, after a strong increase of the internal stress at small strains ($\bar{\epsilon}^{pl}$<0.04), the slope of the curves changes drastically due to begin of the inelastic behaviour of the cementite phase. The evolution of

the mixing and subsequently of the total internal stress is different for both steel grades: for the reference 18CrNiMo7-6 alloy, X' and X continue to growth slowly and reach a stress plateau at large strains ($\bar{\epsilon}^{pl}$>0.4); whereas for the substitute grade they present a max. at $\bar{\epsilon}^{pl}$=0.18 and then decrease slowly. This different behaviour is due to *the larger kinematic recovery coefficients* k_2 , identified for the ferrite phase of the substitute grade (matrix and ferrite layer of pearlite), than those for the reference alloy (see tables 7 and 8 and fig. 8). Eventually, both intrinsic pearlitic contributions X'' saturate rapidly at $\bar{\epsilon}^{pl}$>0.1 but at a different level: X''=143.77 MPa (reference) and X''=188.40 MPa (substitute). Compared to the reference value, an increase of 31% is observed, which is due to the smaller interlamellar spacing of the substitute pearlite.

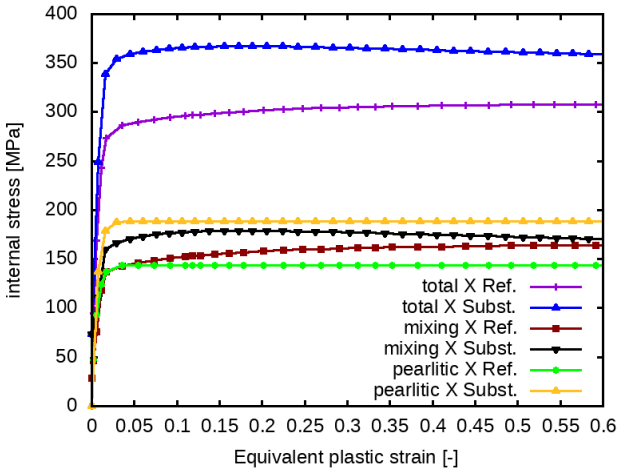

Figure 14: Variation of the effective total internal stress X, the mixing contribution X' and the intrinsic pearlitic contribution X'' as function of the plastic strain for the reference and substitute alloys.

Conclusions

A multiscale approach, based on a two-level homogenisation scheme, is applied here successfully to predict the effective elasto-plastic behaviour of two ferrite-pearlite gear steels, from the knowledge of their microstructure and the properties of their constituents. To efficiently describe the influence of the characterized microstructure on the hardening behaviour of both gear steel grades, an extension of the physically based Delincé et al. KME model [11] has been developed by introducing a nonlinear dependence of the mean free dislocation path *D* on the equivalent plastic strain. Based on a sensitivity analysis, a least-square fit with an experimental stress-strain curve allows to determine the most relevant material parameters of the ferrite matrix and ferrite layer in pearlite. The homogenisation of the pearlite bi-lamella RVE at the nanoscale reveals that pearlite has a pronounced effective anisotropic elasto-plastic behaviour caused by the anisotropy of the cementite phase. Moreover, the homogenization of the ferrite matrix doted either with small MnS inclusions (18CrNiMo7-6 grade) or NbC carbides (substitute grade) at the nanoscale allows for an efficient homogenisation of the ferrite-pearlite microstructure at the microscale by considering there the ferrite matrix as a homogeneous effective phase. The so numerically derived macroscopic flow curves from the respective RVE micromechanical model of each steel grade constitute the basis for

the derivation of a generalized Johnson-Cook hardening law, used in cutting simulations in the 2nd part of this work.

To improve in a near future the model predictions with this homogenisation procedure, more delicate experimental characterisation, compression tests at different strain rate and temperatures and an inverse modelling strategy has to be applied in order to tackle unknown micromechanical model parameters of each phase (ρ_0, C_SS, w, λ^*, …) and to quantify their strain rate and temperature dependence.

Acknowledgments

The authors would like to thank the Deutsche Forschungsgemeinschaft (DFG) for the funding support provided to develop the present work in the project Cluster of Excellence "Internet of Production" (project: 390621612). Moreover, the authors will thank colleagues of a precedent Cluster of Excellence initiative at Aachen University, namely J. Dierdorf (Institute of Metal Forming) and V. Kripak (Department of Ferrous Metallurgy) who have performed the compression tests and the microstructure characterization of both steel gear grades respectively.

Data availability statement

The raw and processed data required to reproduce these findings cannot be shared at this time as the data forms part of the ongoing 2nd part of the present study.

References

[1] S. Konovalov, U. Prahl: "Tailoring the microstructure for micro-alloyed carburizing steels by an ICME approach" in "Fundamentals and Applications of Mo and Nb Alloying in High Performance Steels", Volume 2, Ed. H. Mohrbacher, TMS, 2015, pp. 215-225.

[2] L. Koschmieder, S. Hojda, M. Apel, R. Altenfeld, Y. Bami, C. Haase, M. Lin, A. Vuppula, G. Hirt, G. Schmitz: „AixViPMaP® - an operational platform for microstructure modelling workflows", Integrating Mat. Manuf. Innov., vol. 8, n° 2, 122-143, 2019.

[3] Schmitz J, Prahl U. "Integrative Computational Materials Engineering - Concepts and Applications of a Modular Simulation Platform". Wiley VCH, Germany, 2012.

[4] G. Laschet, P. Fayek, T. Henke, H. Quade, U. Prahl: "Derivation of anisotropic flow curves of ferrite-pearlite pipeline steel via a two-level homogenization scheme". Mat. Scien. & Engng. A vol. 566, pp. 143-156, 2013.

[5] M. Abouridouane, G. Laschet, V. Kripak, A Texeira, J. Dierdorf, U. Prahl, F. Klocke : « Cutting simulations of two gear steels with microstructure dependent material laws", Procedia CIRP, vol. 58, pp. 549-554, 2017.

[6] I. Gutierrez, A. Altuna: "Work hardening of ferrite and microstructure based modelling of its mechanical behaviour under tension", Acta Materialia, vol. 56, pp. 4682-4690, 2008.

[7] U. Kocks and H. Mecking: "Physics and phenomelogy of strain hardening: the FCC case". Prog. Mat. Science, vol. 48, n° 1, pp. 171-273, 2003.

[8] Y. Estrin, H. Mecking: "A unified phenomelogical description of work hardening and creep based one-parameter models", Acta Metallurg., vol. 32, n°1, pp. 57-70, 1984.

[9] C. Sinclair, W. Poole, Y. Bréchet: “A model for the grain size dependent work hardening of copper”, Scripta Mater., vol. 55, pp. 739-742, 2006.

[10] J. Bouquerel, K. Verbeken, B. De Cooman: „Microstructure-based model for static mechanical behaviour of multiphase steels“, Acta Materialia, vol. 54, pp. 1443-1456, 2006.

[11] M. Delincé, Y. Bréchet, J. Embury, M. Geers, P. Jacques, T. Pardoen: “Structure-property optimization of ultrafine-graided dual-phase steels using a microstructure-based strain hardening model”, Acta Materialia, vol. 55, pp. 2337-2350, 2007.

[12] K. Hariharan F. Barlat: “Modified Kocks-Mecking-Estrin model to account nonlinear strain hardening”, Metallurg. and Mat. Trans. A, vol. 50A, pp. 513-517, 2019.

[13] O. Bouaziz: “Revisited storage sand dynamic recovery of dislocation density evolution law: toward a generalized Kock-Mecking model of strain hardening”, Adv. Engng. Mat., vol. 14, n°9, pp. 759-761, 2012.

[14] F. Barlat, M. Glasov, J. Brem, D. Lege: “A simple model for dislocation behaviour, strain and strain rate hardening evolution in deforming aluminium alloys“, Int. Jnl. of Plasticity, vol. 18, n°7, pp. 919-939, 2002.

[15] B. Berisha, C. Raemy, C. Becker, M. Gorji, P. Hora: “Multiscale modelling of failure initiation in a ferritic-pearlitic steel”, Acta Materialia, vol. 100, pp. 191-201, 2015.

[16] F. Roters, M. Diehl, P. Shantraj, P. Eisenlohr et al.: „DAMASK – the Düsseldorf Advanced Material Simulation Kit for modelling multi-physics crystal plasticity, thermal and damage phenomena from the single crystal up to the component scale“, Comput. Mat. Science, vol. 158, pp. 420-478, 2019.

[17] S. Allain, O. Bouaziz: “Microstructure based modelling for the mechanical behaviour of ferrite-pearlite steels suitable to capture isotropic and kinematic hardening”, Mat. Sci: and Engng. A, vol. 496, pp. 329-336, 2008.

[18] G. I. Taylor: “The mechanism of plastic deformation of crystals: Part I theory”, Proc. Royal Society London, vol. 145, pp. 362-387, 1934.

[19] N. J. Petch: “The cleavage strength of polycrystals”, J. Iron Steel Inst., vol. 174, pp. 25-28, 1953.

[20] A. Deschamps, Y. Bréchet, C. J. Necker, S. Saimoto, J. D. Embury: “Study of large strain deformation of dilute solid solutions of Al-Cu using channel die compression”, Mat. Sci. Engng. A, vol. 207, pp. 143-152, 1996.

[21] G. Ghosh, G. B. Olson: “The isotropic shear modulus of multicomponent Fe-base solid solutions”. Acta Mater., Vol. 50, pp. 2655-2675, 2002.

[22] H. Chen: “Cyclic partial phase transformations in low alloyed steels: modelling and experiments”, PhD thesis, TU Delft, 2013.

[23] L. Mauger, J. E. Herriman, O. Hellman, S. Tracy, M. Lucas, J. Muñoz, Y. Xiao, B. Fultz: Phonons and elasticity of cementite through the Curie temperature”, Physical Review V, vol. 95, 024308, 2017.

[24] B. W. Koo, Y. J. Chang, S. P. Hong, C. S. Kang, S. W. Jeong, W. J. Nam, I. Park, Y. Lee, K. Oh, Y. Kim: “Experimental measurement of Young’s modulus from single crystalline cementite”, Scripta Mater., vol. 82, pp. 25-28, 2014.

[25] J. Alkorta, J. Gil Sevillano: “Assessment of elastic anisotropy and incipient plasticity in Fe3C by nano-indentation”, Jnl. of Mater. Res., vol. 27, pp. 45-52, 2011.

[26] C. Jiang, S. G. Sirinivasan, A. Caro, S. A. Maloy: “Structural, elastic and electronic properties of Fe3C from first principles”, J. Appl. Phys., vol. 103, n°4, 043502, pp. 1-8, 2008.

[27] I.V. Isaichev, Zh. Tekh. Fiz., vol. 17, pp. 835-838, 1947.

[28] A. Luque, J. Aldazabal, J.M. Martinez-Esnaola, J. Gil Sevillano: “A molecular dynamics of strength of cementite F3C”, Proc. 5th Int. Conf. on Multiscale Material Modelling, P. Gumbsch, E. van der Giessen (Eds.), Freiburg, Germany, pp. 469-472, 2010.

[29] R. Hill, Proc. R. Soc. London, 193, pp. 281-297, 1948.

[30] M. Umemoto, Y. Todaka, T. Takahashi, P. Li, R. Tokumiya, K. Tsuchiya: “High temperature deformation behaviour of bulk cementite produced by mechanical alloying and spark plasma sintering”, Mat. Science and Engng. A, vol. 375-377, pp. 894-898, 2004.

[31] A. Taniyama, T. Takayama, M. Arai and T. Hamada: “Deformation behaviour of cementite in deformed high carbon steel observed by X-ray diffraction with synchrotron radiation”, Metall. and Mat. Trans. A, vol. 48, pp. 4821-30, 2017.

[32] HOMAT v6.0, manual, 2020, https://docs.micress.rwth-aachen.de/homat/homat/homat

[33] O. Kavci, S. Cabuk: “First principles study of structural stability, elastic and dynamical properties of MnS”, Comput. Mat. Science, vol. 95, pp. 99-105, 2014.

[34] F. Matsuno, S. Nishikida, H. Ikesaki: “Mechanical properties of Manganese sulphides in the temperature range between room temperature and 1000°C”, Transactions ISIJ, vol. 25, pp 989-998, 1985.

[35] Digimat version 2019.1, manual, 2019, https://www.e-xstream.com/industry/latest-digimat-release

[36] Y.Z. Liu, Y.H. Jiang, R. Zhou, J. Feng: “First principles study the stability and mechanical properties of MC (M=Ti, V, Zr, Nb, Hf and Ta) compounds”, Jnl. of Alloys and Compounds, vol. 582, pp. 500-504, 2014.

[37] M. Woydt and H. Mohrbacher: “The tribological and mechanical properties of Niobium carbides (NbC) bonded with Cobalt or Fe3Al”, Wear, vol. 321, pp 1-7, 2014.

[38] R. Quey and L. Renversade: “Optimal polyhedral description of 3D polycrystals: method and application to statistical and synchrotron X-ray diffraction data”, Comput. Meth. In Appl. Mech. & Engng., vol. 330, pp. 308-333, 2018.

[39] A. Bouhemadou, R. Khenata, M. Sahnoun, H. Baltache and M. Kharoubi: “First-principles study of structural, elastic and high-pressure properties of cerium chalcogenides”, Physica B, vol. 363, pp. 255-261, 2005.

[40] Gmsh version 4.4.1, 2019, https://gmsh.info

[41] Abaqus R2019, manual, 2019, https://www.3ds.com/products-services/simulia/products/abaqus/

[42] R. Hill: “Elastic properties of reinforced solids: Some theoretical principles”, J. Mech. of Phys. Solids, vol. 11, pp. 357-372, 1963.